Appl. Phys. B 47, 333–342 (1988)

Applied Physics B Photophysics and Laser Chemistry

Verification of a XeCl* Laser Model by Measurement of the Plasma Conductivity

G. Stielow, Th. Hammer, and W. Bötticher

Institut für Plasmaphysik, Universität, D-3000 Hannover, Fed. Rep. Germany

Received 5 April 1988/Accepted 16 June 1988

Abstract. Measurements of current, voltage, and laser emission of an X-ray preionized self-sustained XeCl* laser discharge using Ne:Xe:HCl gas mixtures are compared with predictions of spatially homogeneous model calculations. As a prerequisite an accurate and detailed model of the electrical circuit is developed. For current and voltage measurements electro-optical methods are used. Corrections to the measurements and the reliability of the final data are discussed in detail. Using collision cross sections from the recent literature and stepwise vibrational excitation of HCl up to $v=3$ reproduces the electrical conductivities measured in a large field of parameters. The reliability and numerical stability of the model calculations depend on the way in which the e-HCl collision terms of the Boltzmann equation and the e-HCl collision rates are evaluated. The predicted total laser pulse energies are too small, but the shape and timing of the pulse correspond to the experimental values.

PACS: 42.55G, 52.65, 52.80

In spite of many efforts, a complete model of rare gas halide lasers pumped by a self-sustained discharge is still lacking [1–4]. A complete model should be able to predict the laser emission $P(t)$, voltage $V(t)$ and current $I(t)$ for a given discharge circuit, electrode profile, gas mixture and preionization procedure over a large field of these parameters. Such a model would be very helpful for optimizing large high pressure lasers [5]. The present method of development by stepwise extrapolation will become very expensive for these lasers.

The most simple model conceivable makes the following assumptions:

1. The discharge is absolutely homogeneous, i.e. the preionization density n_{e0}, current density j, electric field strength E as well as gas density and composition do not depend on a spatial coordinate. One has a spatially homogeneous model.

2. The current I delivered from the circuit flows into a cross-section $A=l\cdot b$ of the discharge. A is an input data value to be taken from experiment. We will include the possibility that A changes in time, but $A(t)$ is again an input to the model. Thus one always has $I=j\cdot A$.

3. The voltage drop V_D in the discharge is related to E by $V_D=E\cdot d$, d being the electrode distance.

In all models available today it is assumed that the mean distance $n_{e0}^{-1/3}$ between the preionization electrons is so small that the structure of the individual avalanches are smeared out [6–8].

The most important deficits of such a spatially homogeneous model are the neglect of the following:

a) space charges producing a cathode fall,

b) field inhomogenities due to the electrode profiles,

c) macroscopic spatial inhomogenities of the preionization.

In this paper we present a spatially homogeneous model for a XeCl* laser, which makes use of a numerical code developed by Chow et al. [9] and Rockwood [10], and compare its predictions with experimental findings in a XeCl* laser discharge.

We have investigated an X-ray preionized small laser, which is a modification of the type EMG 50 from Lambda Physik. X-ray preionization does not depend on impurities always present in the laser gas mix. Thus compared to UV preionization by spark arrays in the laser head, one will have a more reproducible preioniza-

tion when changing the gas composition. Due to the strong interaction between discharge and electrical circuit, a very careful analysis of this circuit and the methods for measuring I and V has been made. In our opinion experimental checks of model predictions are meaningless without a detailed knowledge of the exact circuit data and the measuring methods.

We will discuss the reactions included into our model and give the cross-sections and rate coefficients used; these have been collected from the most recent literature.

The model and the circuit data derived will be used in a subsequent paper in which the predicted number densities of excited Xe atoms are compared with experimental values deduced from the absorption of tunable dye laser radiation [11, 12].

1. Model of the Discharge Plasma

The model calculates from the existing electrical field $E=V/d$ and existing particle densities, the electron distribution function EDF by a numerical solution of the Boltzmann equation. From the EDF one gets the electron mobility μ, the electron drift velocity $v_d=\mu\cdot E$ and the current density $j=e\cdot n_e\cdot v_d=I/A$. Due to the reactions in the plasma n_e and v_d and thus I change in time. This again changes the voltage drop in the electrical circuit, resulting in a change of the electric field E in the discharge. In the next time step the calculation is repeated with the new value of E. The width of the time step Δt can be changed during the calculation and is controlled by the changes of all particles and circuit variables. Running on a CRAY X-MP the code including the reaction kinetic model, the Boltzmann code and the circuit model described below needs 100 s cpu time for a discharge duration of 125 ns. The compilation time is about 2 s.

1.1. *Calculation of the* EDF

For the solution of the Boltzmann equation the code uses the procedure given by Rockwood [10]. It includes inelastic collisions with excited states and superelastic collisions, which both turn out to be very important. The electron energy grid is made up of 100 equidistant points ε_j. The upper limit of the energy is chosen such that the last value of the EDF is about 10^{-7}/eV.

In the original version of this code the collision rates for the electron collisions are calculated from the EDF by interpolation of the cross-sections $Q(\varepsilon)$ to the grid of the EDF $f(\varepsilon)$

$$R(t)=\Sigma_j v(\varepsilon_j)\cdot Q(\varepsilon_j)\cdot f(\varepsilon_j)\cdot \Delta\varepsilon$$

with the speed of the electrons

$$v(\varepsilon_j)=(2\varepsilon_j/m_e)^{1/2}.$$

Especially in the case of dissociative attachment to HCl, the cross-sections show strongly peaked structures within one energy interval of the EDF which can become very important for the calculation of the reaction rates. So we take a mean value of the cross-section calculated according to

$$Q(\varepsilon_j)=\frac{\Sigma_{\varepsilon_{j-1}<\varepsilon_l\leqq\varepsilon_j} Q(\varepsilon_l)\cdot v(\varepsilon_l)\cdot f(\varepsilon_l)\cdot \Delta\varepsilon_l}{\Sigma_{\varepsilon_{j-1}<\varepsilon_l\leqq\varepsilon_j} v(\varepsilon_l)\cdot f(\varepsilon_l)\cdot \Delta\varepsilon_l}$$

instead of the interpolated one. Within the interval $(\varepsilon_{j-1},\varepsilon_j)$ the EDF is not assumed to be constant but interpolated to the grid points ε_l of the collision cross-section. Using this procedure and a grid of 50 points for the EDF instead of 100 does not change the model predictions by more then 10%.

Electron-electron collisions, which may be important for the Maxwellisation of the EDF, are not included in the present model. We hope that due to the large rate of the superelastic collisions the effect of the e–e collisions is small. Work is underway to check this assumption.

1.2. *Reactions Included*

The principal reaction routes that determine the plasma conductivity and the laser pulse are shown in Fig. 1. The full set of reactions used for our model calculations can be seen from Table 1. Elastic e–He collisions (2) are included to estimate the effect of Helium admixtures to the discharge medium on the plasma conductivity. Because of their high excitation energy, inelastic e–He collisions can be neglected.

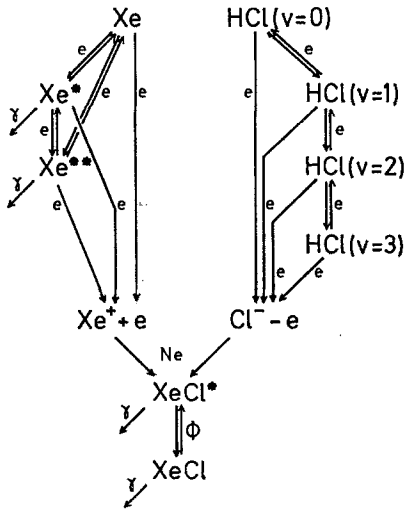

Fig. 1. Reaction scheme of the XeCl* laser. e stands for electron-collision reactions, γ for quenching and Φ for absorption and induced emission of laser photons

Table 1. Reactions, collision cross sections*, and rate constants used for our model calculations

Elastic electron collisions				
(1)	$e + Ne \rightarrow e + Ne$	0 – 2.18 eV	O'Malley, Crompton	[17]
		5 –200 eV	Fon, Berington	[18]
(2)	$e + He \rightarrow e + He$	0 – 12 eV	Nesbet	[19]
		12 – 50 eV	Fon et al.	[20]
(3)	$e + Xe \rightarrow e + Xe$	0.01– 20 eV	Sin Fai Lam	[21]
		20 –200 eV	Hayashi	[22]
(4)	$e + HCl \rightarrow e + HCl$	0.01– 10 eV	Padial, Norcross	[23]
Electron collision excitation				
(5,6)	$Xe + e \rightleftharpoons Xe^* + e$	8.32–100 eV	Hayashi	[22]
			Fel'tsan, Zapesochnyi	[24]
(7,8)	$Xe + e \rightleftharpoons Xe^{**} + e$	9.57–100 eV	Fel'tsan, Zapesochnyi	[24]
(10,11)	$Xe^* + e \rightleftharpoons Xe^{**} + e$	1.42– 42.5 eV	Hyman	[25]
(14,15)	$Ne + e \rightleftharpoons Ne^* + e$	16.3 – 21.5 eV	Schaper, Scheibner	[26]
		30 –200 eV	de Heer et al.	[27]
(18,19)	$HCl\ (v=0) + e \rightleftharpoons HCl\ (v=1) + e$	0.35– 5.0 eV	Rohr, Linder	[28]
			Domcke, Mündel	[16]
(20,21)	$HCl\ (v=0) + e \rightleftharpoons HCl\ (v=2) + e$	0.67– 5.0 eV	Rohr, Linder	[28]
			Domcke, Mündel	[16]
(22,23)	$HCl\ (v=1) + e \rightleftharpoons HCl\ (v=2) + e$	0.35– 5.0 eV	(18,19)·2 following Dem'yanov et al.	[4]
(24,25)	$HCl\ (v=0) + e \rightleftharpoons HCl\ (v=3) + e$	0.99– 5.0 eV	Domcke, Mündel	[16]
(26,27)	$HCl\ (v=1) + e \rightleftharpoons HCl\ (v=3) + e$	0.67– 5.0 eV	(20,21)·2	
(28,29)	$HCl\ (v=2) + e \rightleftharpoons HCl\ (v=3) + e$	0.35– 5.0 eV	(18,19)·3 following Dem'yanov et al.	[4]
Electron collision ionization				
(9)	$Xe + e \rightarrow Xe^+ + 2e$	12.13–140 eV	Rapp, Englander-Golden	[29]
(12)	$Xe^* + e \rightarrow Xe^+ + 2e$	3.81–100 eV	Hyman	[30]
(13)	$Xe^{**} + e \rightarrow Xe^+ + 2e$	2.39–100 eV	Hyman	[30]
(16)	$Ne + e \rightarrow Ne^+ + 2e$	21.6 –200 eV	Rapp, Englander-Golden	[29]
(17)	$Ne^* + e \rightarrow Ne^+ + 2e$	4.94–100 eV	Hyman	[30]
Dissociative attachment				
(30)	$HCl\ (v=0) + e \rightarrow H + Cl^-$	0.80–2.40 eV	Orient, Srivastava	[14]
			Domcke, Mündel	[16]
(31)	$HCl\ (v=1) + e \rightarrow H + Cl^-$	0.45–1.96 eV	Domcke, Mündel	[16]
(32)	$HCl\ (v=2) + e \rightarrow H + Cl^-$	0.10–1.46 eV	Domcke, Mündel	[16]
(33)	$HCl\ (v=3) + e \rightarrow H + Cl^-$	0.02–1.20 eV	Bardsley, Wadehra	[31]
Penning and associative ionisation				
(55)	$Ne^* + Xe \rightarrow NeXe^+ + e$	$2.3 \cdot 10^{-17}$ m^3/s	Neynaber, Tang	[32]
(56)	$Ne^* + Xe \rightarrow Ne^+ + Ne + e$	$7.5 \cdot 10^{-17}$ m^3/2	Neynaber, Tang	[32]
Excited xenon neutral particle collisions				
(35)	$Xe^* + HCl \rightarrow Xe + H + Cl$	$5.6 \cdot 10^{-16}$ m^3/s	Velazco et al.	[33]
(40)	$Xe^* + HCl\ (v=1) \rightarrow XeCl^* + H$	$2.0 \cdot 10^{-16}$ m^3/s	Chang	[34]
(36)	$Xe^{**} \rightarrow Xe^* + h\nu$	$36.2 \cdot 10^6$/s	Aymar, Coulombe	[35]
(37)	$Xe^{**} + HCl \rightarrow XeCl^* + H$	$4.2 \cdot 10^{-16}$ m^3/s	Ku, Setser	[36]
(39)	$Xe^{**} + HCl \rightarrow Xe + H + Cl$	$3.8 \cdot 10^{-16}$ m^3/s	Ku, Setser	[36]
(38)	$Xe^{**} + Xe \rightarrow Xe + Xe$	$9.7 \cdot 10^{-17}$ m^3/s	Böwering et al.	[37]

* The middle column gives the energy range for which data of the given reference were used

Table 1 (continued)

XeCl* formation and quenching				
(34)	$Xe^+ + Cl^- + Ne \rightarrow XeCl^* + Ne$		Flannery	[38]
(57)	$NeXe^+ + Cl^- \rightarrow XeCl^* + Ne$	$2.0 \cdot 10^{-12}$ m^3/s	Levin et al.	[39]
(44)	$XeCl^* + Ne \rightarrow Xe + Cl + Ne$	$3.3 \cdot 10^{-19}$ m^3/s	Finn et al.	[40]
(45)	$XeCl^* + Xe \rightarrow Xe + Cl + Xe$	$2.1 \cdot 10^{-18}$ m^3/s	Levin et al.	[39]
(46)	$XeCl^* + HCl \rightarrow Xe + Cl + HCl$	$7.7 \cdot 10^{-16}$ m^3/s	Levin et al.	[39]
(47)	$XeCl^* + e \rightarrow Xe + Cl + e$	$3.0 \cdot 10^{-13}$ m^3/s	Wang	[2]
XeCl quenching				
(51)	$XeCl + Ne \rightarrow Xe + Cl + Ne$	$2.4 \cdot 10^{-18}$ m^3/s	Wang	[2]
(52)	$XeCl + e \rightarrow Xe + Cl^-$	$7.0 \cdot 10^{-14}$ m^3/s	Wang	[2]
Emission and absorption of laser photons				
(42)	$XeCl^* \rightarrow XeCl + h\nu$	$90.0 \cdot 10^6$/s	Hay, Dunning Inoue et al.	[41] [42]
(43)	$XeCl^* \rightarrow XeCl + \Phi$	4.40/s	beam divergence	
(41)	$XeCl^* + \Phi \rightarrow XeCl + 2\Phi$	$1.3 \cdot 10^{-11}$ m^3/s	Brau	[43]
(50)	$XeCl + \Phi \rightarrow XeCl^*$	$1.3 \cdot 10^{-11}$ m^3/s	absorption- equal to emission line profile assumed	
(53)	$Cl^- + \Phi \rightarrow Cl + e$	$9.6 \cdot 10^{-14}$ m^3/s	includes various other absorption reactions	
Other reactions				
(54)	$Ne^+ + Xe + Ne \rightarrow NeXe^+ + Ne$	$1.0 \cdot 10^{-43}$ m^6/s	Levin et al.	[39]
(48)	$H + Cl^- \rightarrow HCl + e$	$9.7 \cdot 10^{-16}$ m^3/s	Wang	[2]
(49)	$H + Cl + Ne \rightarrow HCl + Ne$	$1.1 \cdot 10^{-45}$ m^6/s	Bruzzese	[44]

Compared other model calculations [2, 3, 13], XeCl* production and quenching, XeCl quenching and the absorption of laser photons are taken into account in the present model with a few example reactions only. This limitation is justified, because we are mainly interested in a good description of the plasma conductivity, which is of fundamental importance for a good excimer laser model but only weakly influenced by the laser photon pulse.

A part of the reactions given in Table 1 can usually be neglected: Direct ionization of neon (16), the excimer formation from $NeXe^+$ (57) with its precursors (54, 55) and vibrational excitation of HCl where the vibrational quantum number v changes by more than 1 (20, 24, 26) and the corresponding superelastic collisions (21, 25, 27) are unimportant for the simulation of our laser. On the submicrosecond time scale HCl reformation (48, 49) can be neglected too. From some very recent model tests we conclude that the Xe** quenching reaction (38) should be omitted or changed to $Xe^{**} + Xe \rightarrow Xe^* + Xe$.

If one is interested in the investigation of gas mixtures with very low HCl partial pressure or in the simulation of discharge filamentation due to the HCl depletion instability [14], the formation of molecular ions, i.e. $NeXe^+$ and Xe_2^+, and their dissociative recombination with electrons must be included to give correct values of the electron density. Normally the degree of ionization is determined by multistep ionization of Xe and dissociative attachment to HCl.

A detailed discussion of the kinetic models and of the cross sections used for Xe excitation (5, 7) and for stepwise vibrational excitation and dissociative attachment of HCl (20–29) will be given in a subsequent paper [12]. A complete list of the numerical values actually used is available on request.

2. Model of the Electrical Circuit

The model of the electrical circuit used in our work is shown in Fig. 2. Its very detailed structure turned out to be necessary to reproduce the measured discharge current by the model calculations. The ignition of the thyratron is simulated by a resistance, which drops linearly from 30 Ω to 0.01 Ω within 15–30 ns. This fall time depends on the starting voltage and the working conditions of the thyratron. After ignition $R_{thy} = 0.01\ \Omega$ is assumed. This assumption is not critical since in the present circuit model R_{thy} after ignition is only a small part of $\hat{R}$, which is the value fitted to the measurements.

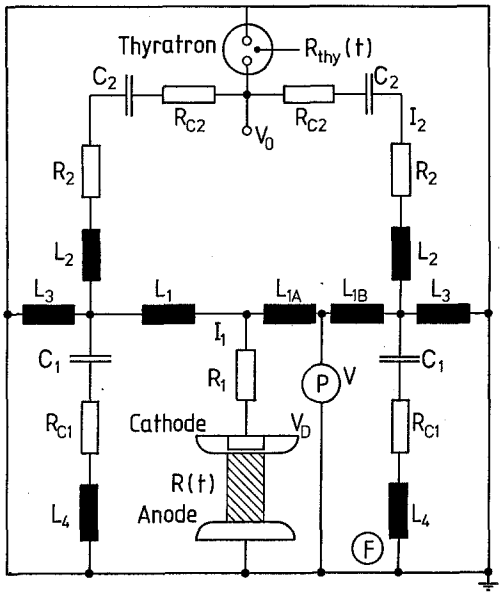

Fig. 2. Model of the electrical circuit of the EMG 50. The values of the capacitances, inductances, and resistivities are $C_1 = 4.3$ nF, $C_2 = 10.3$ nH, $L_1 = 15$ nH, $L_2 = 94$ nH, $L_3 = 100$ µH, $L_4 = 5.0$ nH, $R_1 = 10$ mΩ, $R_2 = 60$ mΩ, $R_{C1} = 80$ mΩ, $R_{C2} = 0.44$ Ω. P and F give the locations of the Pockels cell and the Faraday probe. The circuit model can be simplified by taking into account only one half of the feeding circuit, multiplying the values of the capacitances by two and the values of inductances and resistances by one half

For C_1 and C_2 ceramic capacitors are used (C_1: MURATA, C_2: TDK), whose capacitances show a strong dependence on voltage and on frequency. We measured the frequency dependence up to 10 MHz and found it to be of the same magnitude as the voltage dependence but directed oppositely. R_1 and R_2 represent skin-effect and contact resistances.

The values $L_2 + L_4$ and $\hat{R} = 0.5 \cdot (R_{C1} + R_{C2} + R_2) + R_{thy}$ have been chosen such that model calculations reproduce the voltage signals measured under conditions for which the laser discharge does not ignite (this can be achieved using only the buffer gas instead of the complete mixture). The surprisingly large value of $\hat{R} = 0.3$ Ω after ignition of the thyratron is believed to be caused by the ohmic losses R_{C1} and R_{C2} in the ceramic capacitors. In particular, the necessity to give R_{C1} a value different to zero corroborates this assumption. Additionally we found that the frequency dependence of the capacitors could be simulated by reducing the voltage dependence to 40% of the value given by the manufacturer.

$L_1 + L_4$ was taken from the resonance frequency of a dummy of the laser head. Its value was later on confirmed by the measurement of the discharge current I_1. The ratio of R_{C1} and R_{C2} was chosen such that the zeros and the first minimum of I_1 were reproduced by the model.

Also shown in Fig. 2 is the location of a Faraday probe F and a Pockels cell P for the measurement of a current I_F and a voltage V_p near the discharge. As will be seen in Sect. 3, these are not the current I_1 through the discharge and the voltage drop V_D between the electrodes, which are the magnitudes relevant for model tests.

3. Experiments

The laser head has a gap of 20 mm between flat electrodes of 200 mm length and 40 mm width. All measurements were performed with a discharge having a length of 170 mm and a width of 10 mm, which was the area preionized by the X-ray beam at the cathode. This width coincides with the observed width of the laser pulse and the visible emission. Thus in the model calculations a cross-section of $A = 10 \cdot 170$ mm^2 is used (the discharge homogeneity is discussed in [12]). The X-ray tube is mounted above the cathode between laser head and thyratron, its anode having a distance of about 60 mm to the laser cathode.

The X-ray preionizer uses a Ta knife edge of 10 µm width and 200 mm length as cathode and a gold transmission anode. Its PFN is a Blümlein made up from $2 \cdot 5$ 50 Ω cables of 14 m length. The cables are charged to 20 kV. The X-ray diode is coupled to the Blümlein by a transformer with a core of 3 tori of amorphous metal (6030F, Vakuum Schmelze Hanau, cross-section 7 cm^2, volume 240 cm^3) with a winding ratio of 3:15. Figure 3 shows the voltage, current and X-ray pulse of the system. The X-ray pulse is moni-

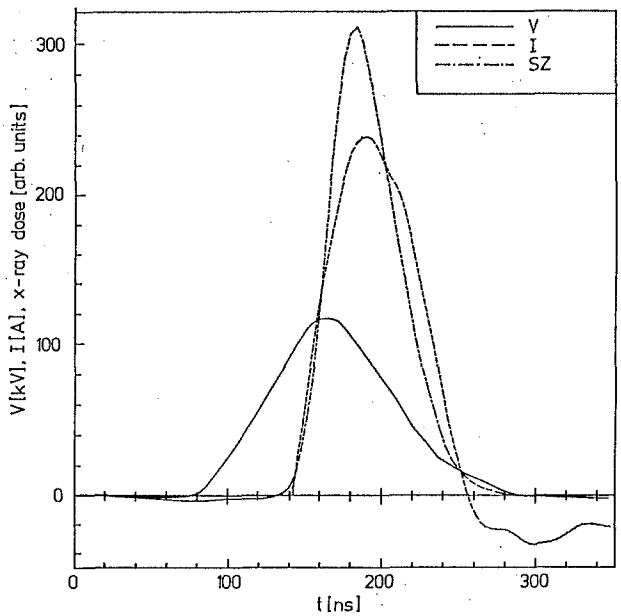

Fig. 3. Current (I), voltage (V) and scintillator output (SZ) of the X-ray preionizer

tored by a lead-loaded scintillator (Nuclear Enterprise, NE 148). The system can be operated at a repetition frequency of up to 200 Hz and has been used for 500000 discharges without any degradation. More details of the laser and preionizer are given by Stielow [45] and Bähr [46].

3.1. Measurement of Voltage and Current

The experimental set-up for time-resolved measurements of current and voltage near the discharge and the laser photon pulse $P(t)$ and measurement of the laser pulse energy $W=\int P(t)dt$ with a GENTEC ED 500 is shown in Fig. 4. Both the electro-optic detectors for current and voltage use a 5 mW He–Ne laser as light source. To minimize electrical noise the laser beams are lead into a screen cage were they are detected by Hamamatsu S 1722 photodiodes. The diode signals are ac-amplified as well as dc-amplified. The ac-amplifier (50 Ω) gives the discharge signal $U_\alpha(t)$, the dc-amplifier (1 MΩ) the light level U_0 at the working point of the detector on a digital voltmeter. All detectors have a time resolution of better than 2 ns. To correlate the time scales of the oscilloscopes (HP 1727A, Tektronix 7488), a time mark is superimposed on all ac-signals.

The Faraday probe is a glas rod (Schott glass SF 57, length 200 mm, diameter 6 mm) with a Verdet constant of $V_e=2.522\cdot 10^{-5}$ rad/A at $\lambda=632.8$ nm.

The Pockels probe is a quartz crystal of $19.6\times 63.5\times 13.7$ mm^3 [47]. In contrast to the system of Ballik [48], the laser beam transverses in the y-direction and the voltage is applied in the x-direction. The half-wave voltage of the Pockels probe is $V_\pi=292.2$ kV for $\lambda=632.8$ nm.

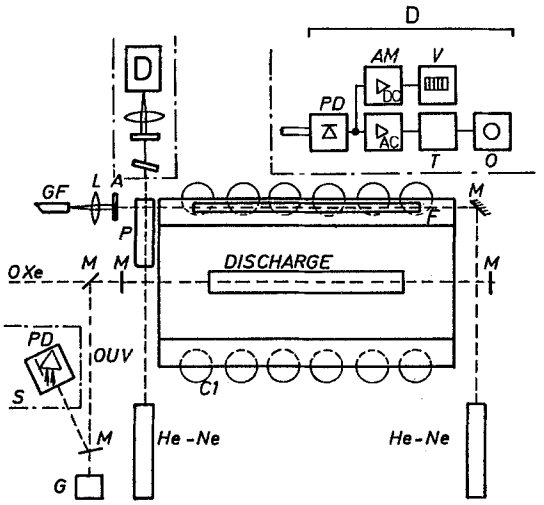

Fig. 4. The experimental set-up. A: analyzer; AM: amplifiers; C: compensation plate; C_1: peaking capacitance; D: detection system; F: Faraday probe; G: GenTec ED 500 energy meter; GF: glass fibre; L: lens; M: beam-splitter or mirror; O: oscilloscope; OUV: optical axis of the UV detecting system; OXe: optical axis of the dye-laser absorption experiment [11, 12]; PD: fast Si-Pin diode; S: screen cage; T: time-mark generator; V: digital voltmeter

The linearly polarized He–Ne beam leaves the quartz elliptically polarized even without an applied voltage. The following compensation plate transforms this to circular polarized light. The ellipticity depends strongly on the temperature of the crystal. To keep the polarization circular we control the angular position between compensation plate and Hĕ–Ne beam by a stepper motor.

The difference between the signal travelling times of Faraday and Pockels probe was measured separately with a 2 ns pulse from a laser diode at $\lambda=904$ nm.

3.2. Theory of Measurements

The voltage V_P and the apparent current I_F are calculated from the output signals of the electro-optic detectors relative to their working points.

For the current I_F seen by the Faraday probe we have

$$I_F=1/V_e\left[\arcsin\frac{U_\alpha(T)}{U_0-1}\right], \tag{1}$$

which correlates to I_1 and I_2 according to

$$I_F=k_1I_1-k_2I_2, \tag{2}$$

where k_1 and k_2 are the geometric coupling factors of I_1 and I_2 into the Faraday probe due to the particular details of our set-up.

The voltage V_P measured by the Pockels cell is given by

$$V_P=2V_\pi/\pi(-\pi/4+\arcsin(0.5[U_\alpha(t)/U_0+1])^{1/2} \tag{3}$$

which comprises three components:

$$V_P=V_D+L_{1A}\dot{I}_1+R_1I_1. \tag{4}$$

As will be shown below the second term on the right-hand side, which represents the unavoidable inductive component, limits the accuracy in the determination of the discharge voltage V_D.

3.3. Analysis of the Measured Data

All measured data are digitized from polaroids with a step width of 0.5% of a division and then analysed on a personal computer. Firstly the baselines of the signals are evaluated as the mean value of the first ten points. Secondly the time axis is linearized. The nonlinearities of the oscilloscopes and distortions by the polaroid cameras are determined by digitizing a very well known sinusoidal signal of 50 MHz. Thirdly the

accuracy of the digitizing process is checked by repeating both the digitizing and the subsequent procedure several times. Fourthly the averaged signals are numerically smoothed by orthogonal polynomials to minimize the errors in calculating the time derivative of I_1 used in (4).

From a set of $I_F(t)$ and $V_P(t)$ data obtained by this procedure, $I_1(t)$ and $V_D(t)$ are calculated. As $I_2(t)$ is taken from the model, the time scales of the experimental data $I_F(t)$ and $V_P(t)$ have to be correlated to those of the model calculation. This is done by shifting the first rise of V_P into the first rise of the modeled V_D, which is justified since, in this part of the discharge, V_P is equal to V_D as $V_D \gg L_{1A}\dot{I}_1 + R_1 I_1$. In that way the jitter of the thyratron, which was about ± 25 ns, is eliminated. On the other hand the formation of the thyratron's discharge reproduced well enough to describe it as a time-dependent ohmic load.

The error introduced by taking I_2 from the model is negligible since I_2 hardly depends on the development of the discharge up to the second zero of I_1 (see I_1 in Fig. 6). To find the value of k_2, I_F is fitted to I_2 in the region of the first rise of V_P for a lot of signals; this gives $k_2 = 0.105 \pm 0.015$. Now $k_1 I_1 = I_F + k_2 I_2$ can be evaluated, which gives a significant shift in the zeros and a reduced depth of the first minimum of $k_1 I_1$ relative to I_F.

The absolute value of I_1 is fitted to the modeled current in the first maximum for a large number of shots of the EMG 50 and gives

$$k_1 = 0.32 \pm 0.01 \text{ or } \pm 3\% .$$

Although $k_2 I_2$ is a small correction it must nonetheless be taken into account. Modeling the circuit of the EMG 50 once to reproduce I_F and once to reproduce $I_F + k_2 I_2$ (relative only, which is done by changing the value of R_{C1}) strongly affects the development of Xe* and Xe**. The measured absorption signals of xenon lines [11, 12] show the importance of adding $k_2 I_2$ to I_F.

Knowing about I_1, V_D can be derived from V_P by (4). Information about L_{1A} follows from the first and second zero of I_1. There $V_D = I_1 = 0$ and so

$$L_{1A} = V_P / \dot{I}_1 .$$

The first current zero gives $L_{1A} = 9.8 \pm 0.6$ nH, the second zero leads to $L_{1A} = 8.3 \pm 1.7$ nH. Shifting I_1 in time slightly so that the values of L_{1A} for both zeros become equal gives $L_{1A} = 9.3 \pm 0.8$ nH. The time shifts were always smaller than twice the error in the time correspondence of I_F and V_P, that is smaller than ± 0.6 ns. At the third zero of I_1 we have $L_{1A} = 9.6 \pm 0.8$ nH for both the shifted and the unshifted case. During this evaluation we have used a time independent k_1.

The time correspondence of I_1 and V_P has a systematic error of ± 0.3 ns and a statistical error of ± 0.4 ns. The amplitude error of both I_1 and V_P at their maximum value is $\pm 3\%$.

4. Results and Discussion

We have measured voltage, current and photon pulse for various gas mixtures, pressures, and loading voltages V_0. Figure 5 gives the range investigated and the first maximum of current I_1 in comparison with the modeled values.

The maximum of I_1 hardly varies with gas mixture and pressure for the higher loading voltages $V_0 = 25$ kV and $V_0 = 30$ kV. This indicates that I_1 is determined by the circuit and not by the discharge. So a measurement of the discharge current has no significance as a check of the discharge model. On the other hand, the current is a very sensitive quantity to control the model of the circuit which essentially determines the temporal development of all calculated data. Thus a careful measurement of the current is absolutely necessary if the discharge model is to be tested by measurements of e.g. excited species [11, 12].

At $V_0 = 15$ kV and $V_0 = 20$ kV and for gas mixtures with high total pressure or high xenon partial pressure, the discharge does not ignite fully before the outer voltage at the capacitor C_1 drops again and so the current I_1 does not reach a value corresponding to the fully burning or quasi-steady-state discharge.

Figure 6 shows, for one special discharge, V_P, I_1, the laser pulse P and V_D together with its errors for a value of $L_{1A} = 7$ nH. Figure 7 shows the voltage V_D for $L_{1A} = 10$ nH and for $L_{1A} = 7$ nH and the current I_1 for

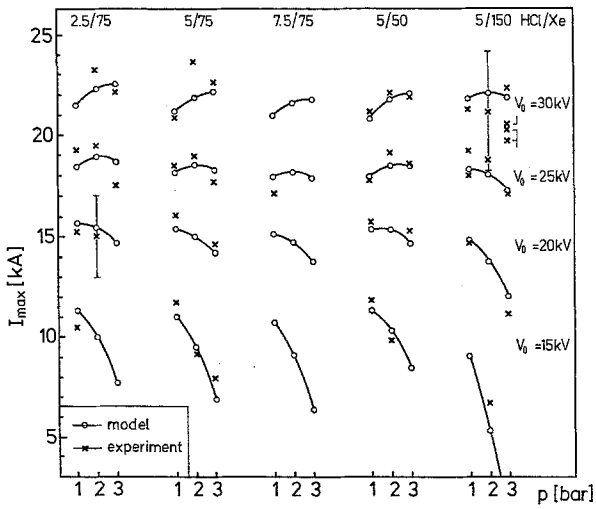

Fig. 5. First maximum of discharge current at different discharge conditions. The parameters above the graphs give the HCL and xenon partial pressures. The error bars are typical for the experimental values

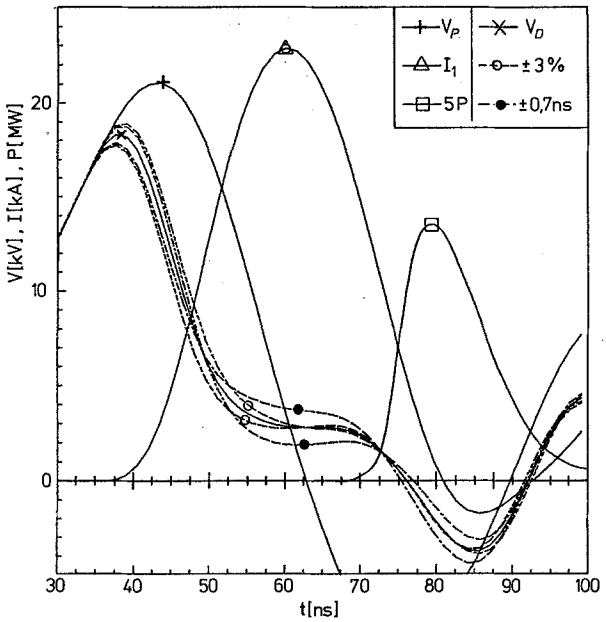

Fig. 6. Measured voltage V_P, discharge current I_1, laser pulse P and discharge voltage V_D (evaluated from V_P using $L_{1A}=7$ nH) with the error bounds of V_D resulting from errors in V_P ($\pm 3\%$) and from errors in the time correlation between V_P and I_1 (± 0.7 ns). $V_0=25$ kV, Ne:Xe:HCl=1920:75:5 mbar

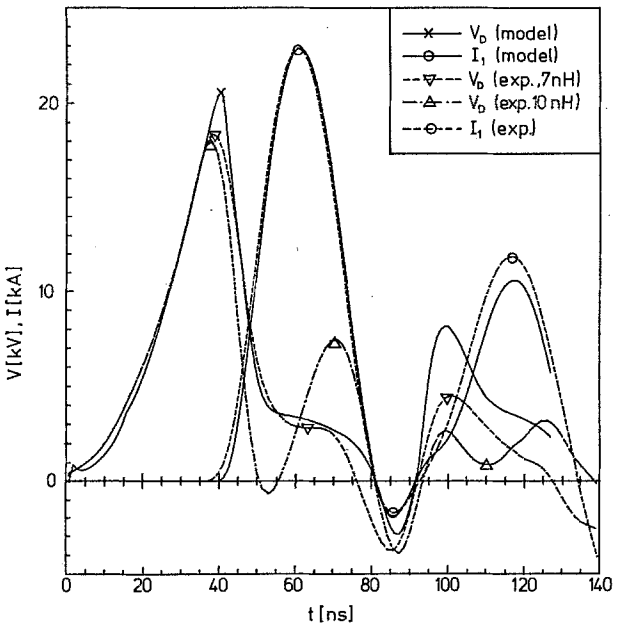

Fig. 7. Comparison between modeled and experimental discharge voltage and current. The two different experimental voltage courses result from different values of the coupling inductance L_{1A} (7 nH and 10 nH)

the same discharge as in Fig. 6 in comparison of experiment and model. $L_{1A}=10$ nH is the coupling inductance for this case when equalizing the values for both zeros of I_1, $L_{1A}=7$ nH gives the best fit of measured V_D to modeled V_D. As can be seen, the discharge voltage shows an extremely strong dependence on the chosen value of the coupling inductance L_{1A}. The value of V_D at the time of the first maximum of I_1 $V_D(I_{max})$ is the most reliable result, as it is independent of L_{1A}. For testing the model predictions we use only this value of V_D.

The model predictions of $V_D(I_{max})$ lie within the errors of measurement for all combinations of gas mixture, pressure and loading voltage measured, when the full HCl kinetics is used (Fig. 1). Reduced versions of the HCl kinetics give values for this voltage much to high and far out of the error bounds [12].

Looking at the full course of $V_D(t)$ in Fig. 7 one sees that the measured and calculated signals agree well for $L_{1A}=7$ nH until shortly after the first maximum of I_1 but then differ. In particular, the first zero of V_D does not coincide with that of I_1, as has to be expected for ohmic behaviour. For $L_{1A}=10.1$ nH, the zeros of V_D and I_1 coincide but the resulting V_D is strongly modulated during the first current half wave. The minimum of V_D at $t=60$ ns) is in contradiction to the steep current rise. Additionally, the measurements of the particle number densities of excited xenon atoms, which are very sensitive to changes in E/N, do not show such a modulation [11, 12].

This discrepancy may be caused by a constriction of the discharge length and width during the drop of I_1 after its first maximum. The corresponding change of the magnetic field distribution in the laser head would change k_1 and alter the measured current. This changes the time derivative of I_1 but not its zeros.

Spatially resolved spectroscopic measurements with our laser [12] indicate a constriction of the discharge area starting after the first current maximum, thus supporting this explanation. This demonstrates that a spatially homogeneous model with constant cross-section A fails at latest in the second half-wave of I_1.

The predicted photon pulse depends strongly on the kind of HCl kinetics used in the code. Only with the full HCl kinetics as given in Fig. 1, do the shape, the time of the maximum and the halfwidth of the photon pulse agree well with the measured ones. The calculated peak powers of the photon pulse differ from the measured ones depending on the discharge parameters given in Fig. 5. Using the otherwise well-adapted kinetics as given by Table 1, the calculated values are much too low. One reason for this disagreement may be that the resonator model used is insufficient for such short laser pulses (turn-around time of the resonator 4 ns, half width of the laser pulse 12 ns). Additionally, we believe that a more sophisticated treatment of the formation and the quenching of the upper and lower laser level and the use of a reliable value of the cross-section for stimulated emission like that proposed by Zhu [13] and Adamovich et al. [49, 50] will give better

agreement. Variations in this part of the kinetics influence neither the multistep ionization nor the HCl kinetics, which are responsible for the temporal development of the conductivity of the discharge and so do not alter the results of this work.

5. Summary

We have investigated the self-sustained glow discharge in a small X-ray preionized XeCl* excimer laser over a large range of Ne:Xe:HCl mixtures, total pressures and charging voltages. The experimental results were used to verify a model of the plasma kinetics. This required a very detailed analysis of the circuit feeding the discharge and of the electro-optical probes measuring current and voltage. Due to the approximately sinusoidal shape of the main current pulse, which is typical for commercial lasers, the inductive correction necessary for the evaluation of the discharge voltage proper was large and limited the accuracy of the results. We want to mention that many reports give uncorrected oscillograms of discharge voltage and current which do not show a voltage zero at current zero. Such data cannot be used to check any model.

The spatially homogeneous model described in this paper reproduced the shape and amplitude of the current as well as of the voltage in the full parameter field within the error bounds of the measurements, i.e. we have a good model for predicting the electrical conductivity.

The model predictions are sensitive to the HCl kinetics. Following the proposal given in [4] we used three vibrational excited states of HCl and stepwise vibrational excitation. Other HCl reaction schemes also found in the literature do not reproduce our measurements. We found that, at first sight, minor changes in the way the collision terms on the right-hand side of the Boltzmann equation and the collision rates for electron-HCl collisions are calculated from the EDF and the corresponding cross-sections, change the numerical stability and the outcome of the model calculations considerably. For comparison of different published models such details have to be known. This may become important when more accurate experimental values are available.

The kinetics in our model has to be developed further to be able to predict the absolute value of the emitted laser energy. This will give only minor changes in the predicted conductivities. In order to check in detail the assumptions made in the calculation of the EDF and the chosen cross-sections, more accurate measurements are needed. These should also give information on the effective cathode fall voltage. Such measurements seem feasible if one uses a discharge and circuit configuration optimized for this purpose and not for high laser power. Of special importance are a long current pulse of constant amplitude and an accurate knowledge of the real distribution of the current density. It is to be expected that for the evaluation of such experiments a two-dimensional model becomes necessary. Such work is in progress.

Spectroscopic measurements of the number densities of excited species give an independent check of the model. Such measurements are reported in a forthcoming paper [12].

Acknowledgements. This work was supported by the Deutsche Forschungsgemeinschaft (Bo 496/11-1, 2 and 3). We thank Lambda Physik, Göttingen, for the permanent loan of the EMG 50 and for financial support during the development of the X-ray pulser. The fast X-ray monitor was developed by M. Bähr. We wish to thank the Institut für Kristallographie, Universität Hannover, for generous help in grinding the crystal.

We are especially grateful to F. Rebentrost, who introduced one of us (G. St.) the code PLASKIN, which was made freely available to us by the Max-Planck-Institut für Quantenoptik, Garching. In running the final model H.-H. Hehmsoth and D. Backhaus were of great help.

References

1. M. Maeda, A. Takahashi, T. Mizunami, Y. Miyazoe: Jpn. J. Appl. Phys. **21**, 1161–1169 (1982)
2. Yuh-Shuh Wang: Ph. D. Dissertation, University of California (San Diego 1982)
3. Hirokazu Hokazono, Katsumi Midorikawa, Minoru Obara, Tomoo Fujioka: J. Appl. Phys. **56**, 680–690 (1984)
4. A.V. Dem'yanov, V.S. Egorov, I.V. Kochetov, A.V. Napartovich, A.A. Pastor, N.P. Penkin, P.Yu. Serdobintsev, N.N. Shubin: Sov. J. Quant. Electron. **16**, 817–820 (1986)
5. Mieko Ohwa, Minoru Obara: J. Appl. Phys. **59**, 32–41 (1986)
6. J.I. Levatter, Shao-Chi Lin: J. Appl. Phys. **51**, 210–222 (1980)
7. G. Herziger, R. Wollermann-Windgasse, K.H. Banse: Appl. Phys. **24**, 267–272 (1981)
8. R.S. Taylor: Appl. Phys. B **41**, 1–24 (1986)
9. W. Chow, K. Hohla, F. Rebentrost: PLF 8, Projektgruppe Laserforschung (Garching 1978)
10. S.D. Rockwood: Phys. Rev. A **8**, 2348–2358 (1973)
11. Th. Hammer, W. Bötticher: Proc. ICPIG XVIII, Contributed Papers, 390–391 (Swansea 1987)
12. Th. Hammer, W. Bötticher: Appl. Phys. B **48** (in press)
13. Sheng-Bai Zhu: Ph. D Dissertation, University of California (San Diego 1984)
14. J. Coutts, C.E. Webb: J. Appl. Phys. **59**, 704–710 (1986)
15. O.J. Orient, S.K. Srivastava: Phys. Rev. A **32**, 2678–2681 (1985)
16. W. Domcke, C. Mündel: J. Phys. B **18**, 4491–4509 (1985)
17. T.F. O'Malley, R.W. Crompton: J. Phys. B **13**, 3451–3464 (1980)
18. W.C. Fon, K.A. Berrington: J. Phys. B **14**, 323–334 (1981)
19. R.K. Nesbet: Phys. Rev. A **20**, 58–70 (1979)
20. W.C. Fon, K.A. Berrington, A. Hibbert: J. Phys. B **14**, 307–321 (1981)
21. L.T. Sin Fai Lam: J. Phys. B **15**, 119–142 (1982)
22. M. Hayashy: J. Phys. D **16**, 581–589 (1983)
23. N.T. Padial, D.W. Norcross, L.A. Collins: Phys. Rev. A **27**, 141–148 (1983)

24. P.V. Fel'tsan, I.P. Zapesochnyi: Ukr. Phys. J. **13**, 143–147 (1968)
25. H.A. Hyman: Phys. Rev. A **24**, 1094–1095 (1981)
26. M. Schaper, H. Scheibner: Beitr. Plasmaphys. **9**, 45–57 (1969)
27. F.J. de Heer, R.H.J. Jansen, W. van der Kaay: J. Phys. B **12**, 979–1002 (1979)
28. K. Rohr, F. Linder: J. Phys. B **9**, 2521–2537 (1976)
29. D. Rapp, P. Englander-Golden: J. Chem. Phys. **43**, 1464–1479 (1965)
30. H.A. Hyman: Phys. Rev. A **20**, 855–859 (1979)
31. J.N. Bardsley, J.M. Wadehra: J. Chem. Phys. **78**, 7227–7234 (1983)
32. R.H. Neynaber, S.Y. Tang: J. Chem. Phys. **70**, 4272–4276 (1979)
33. J.E. Velazco, J.H. Kolts, D.W. Setser: J. Chem. Phys. **69**, 4357–4373 (1978)
34. R.S.F. Chang: J. Chem. Phys. **76**, 2943–2948 (1982)
35. M. Aymar, M. Coulombe: At. Data Nucl. Data Tables **21**, 537–566 (1978)
36. J.K. Ku, D.W. Setser: Appl. Phys. Lett. **48**, 689–691 (1986)
37. N. Böwering, M.R. Bruce, J.W. Keto: J. Chem. Phys. **84**, 715–726 (1986)
38. M.R. Flannery, T.P. Young: Appl. Phys. Lett. **32**, 327–329 (1978)
39. L.A. Levin, S.E. Moody, E.L. Klosterman, R.E. Center, J.J. Ewing: IEEE J. QE-**17**, 2282–2289 (1981)
40. T.G. Finn, R.S.F. Chang, L.J. Palumbo, L.F. Champagne: Appl. Phys. Lett. **36**, 789–791 (1980)
41. P.J. Hay, T.H. Dunning: J. Chem. Phys. **69**, 2209–2220 (1978)
42. G. Inoue, J.K. Ku, D.W. Setser: J. Chem. Phys. **80**, 6006–6019 (1984)
43. Ch.A. Brau in Ch.K. Rhodes (ed.): *Excimer Lasers*, 2nd edn. (Springer, Berlin, Heidelberg 1984) pp. 87–137
44. R. Bruzzese: Lett. Nuovo Cimento **40**, 45–52 (1984)
45. G. Stielow: Dissertation, Universität Hannover (Hannover 1987)
46. M. Bähr, G. Stielow, W. Bötticher: Proc. ICPIG XVIII, Contributed Papers, 386–387 (Swansea 1987)
47. R.S. Ahrens: Diploma thesis, Universität Hannover (Hannover 1985)
48. E.A. Ballik, D.W. Liu: IEEE J. QE-**19**, 1166 (1983) (1983)
49. V.A. Adamovich, V.Yu. Baranov, V.V. Likhanskii, D.D. Malyuta, A.P. Napartovich, Yu.B. Smakovskii, A.B. Strel'tsov: Sov. J. Quant. Electron. **16**, 1463–1466 (1986)
50. V.A. Adamovich, V.Yu. Baranov, A.A. Deryugin, I.V. Kochetov, D.D. Malyuta, A.P. Narpatovich, Yu.B. Smakovskii, A.P. Streltsov: Sov. J. Quant. Electron. **17**, 45–48 (1987)